



Identifying the forefront of electrocatalytic oxygen evolution reaction: Electronic double layer

Guangfu Li*, Po-Ya Abel Chuang*

Department of Mechanical Engineering, University of California, Merced, CA, 95343, United States



ARTICLE INFO

Keywords:

Oxygen evolution reaction
Electronic double layer
Pseudocapacitance
Interfacial reconstruction
Electrocatalysis

ABSTRACT

Developing a fundamental understanding of oxygen evolution reactions (OER) is essential to advancing state-of-the-art energy conversion and storage technologies such as electrolysis. However, it is extremely difficult to directly observe the forefront of the reaction interface, i.e. the electronic double layer (EDL). Herein, electrochemical diagnostic tools are developed to study interfacial behaviors during alkaline OER. Using the traditional linear sweep voltammetry method, we observe that increasing the potential scan rate improves the performance of amorphous Ir oxides, while, for cubic NiCo_2O_3 with higher mass-transport resistance, the effect of scan rate is reversed. The results further confirm that the EDL capacitive and pseudocapacitive processes have a significant impact on electrocatalytic OER. Moreover, continuous EDL reconstruction is observed from double-potential-step chronoamperometry. This reconstruction, mainly caused by chemical phase modification, has a positive influence on OER performance for the Ni-Co oxide, but a negative influence for the Ir oxide. By studying EDL effects, our findings open up new strategies to design promising catalysts and elucidate OER mechanisms.

1. Introduction

With the prospect of ice-free arctic summers on the horizon, scientists worldwide are seeking clean energies to replace traditional fossil fuels [1]. Hydrogen, a zero-emission fuel, is widely considered to be the best alternative to petroleum. Water electrolysis is known as the only practical approach for large-scale hydrogen production from renewable energy sources [2]. In alkaline media, non-noble metal materials can serve as electrocatalysts for both oxygen (OER) and hydrogen (HER) evolution reactions, thus greatly reducing material costs [3–7].

OER is typically the principal focus of research because of its sluggish kinetics, sophisticated reaction mechanisms and insufficient stability of catalyst materials, compared to HER [8–11]. Research interest in OER electrocatalysis has grown with the development of alkaline anion electrolyte membrane electrolysis technology [5,12,13]. Many catalyst candidates with novel performance have been successfully identified by various research groups. However, developing electrochemical benchmarking experiments to effectively characterize these catalysts for OER is only in the early stages [4,14–17]. In non-steady electrochemical experiments, testing sensitivity increases with electrochemical reaction rate [18]. If electroactive species adsorption varies during the process, key parameters, such as potential window and scan rate, for a given electrochemical technique need be modified to account

for the change of the reactive species at the electrode surface [18]. In addition, the stability of most OER catalysts is inversely proportional to their activity [19,20]. In practical applications, the electrocatalysts used are generally based on a compromise between activity and stability [21]. It is therefore important to develop state-of-the-art catalysts for OER that can meet both performance and cost targets. Up-to-date, there are very few systematic design principles that can guide such efforts.

As a heterogeneous reaction in liquid electrolyte, OER occurs only at the interface between the catalyst layer surface and adjacent electrolyte [19]. In alkaline media, the interaction between adsorbed OH^- and the charged electrode surface occurs in the electronic double layer (EDL) which has the ability to store charge in response to unsteady interfacial potential [18]. At the forefront of reaction interface, the formed EDL serving as a capacitor/pseudocapacitor has a complex and unknown microstructure during the electrochemical process due to the chemical and structural flexibility of oxide materials [22]. The species transport resistances in EDL are responsible for the overpotential and increased electrical energy losses. Extensive effort has been made to characterize the key factors that influence interfacial transport behaviors. However, there are several technical gaps, including but not limited to: 1) determining the charging capacitive/pseudocapacitive current, 2) understanding the ionic properties of interfacial host materials, and 3)

* Corresponding authors.

E-mail addresses: gli27@ucmerced.edu (G. Li), abel.chuang@ucmerced.edu (P.-Y.A. Chuang).

<https://doi.org/10.1016/j.apcatb.2018.08.037>

Received 10 April 2018; Received in revised form 8 August 2018; Accepted 15 August 2018

Available online 18 August 2018

0926-3373/ © 2018 Elsevier B.V. All rights reserved.

detecting the large potential gradients in the atomic-scale distance, which in turn drives unpredictable chemical and structural rearrangement [12,22]. In addition, interfacial ion mobility and adsorption has a significant impact on catalyst activity and adsorbate-adsorbate interactions, which in turn determine the OER efficiency. The EDL thickness is generally a few hundred angstroms and is determined mostly by the interaction of the catalysts and the ionic species [18,23]. Real-time in-situ visualization of the EDL information is currently a grand challenge. As a result, there is no EDL model to enable us to accurately capture and predict the interfacial electrochemical behaviors.

The goal of this work is to characterize EDL performance and structure based on representative electrochemical techniques. A thin-film rotating ring disk electrode (TF-RRDE) method is developed and used as an in-situ tool to investigate various interfacial-dependent behaviors. The results demonstrate that capacitive and pseudocapacitive processes and continuous EDL reconstruction are key factors responsible for difficulties in determining actual catalyst performance. Understanding and utilizing EDL charging and reconstruction favorably may lead to new opportunities for developing novel OER electrocatalysts.

2. Experimental section

2.1. Chemicals

Potassium hydroxide (KOH, $\geq 90\%$), anhydrous ethanol ($\geq 95\%$), Nafion[®] solution (5%) and nickel(II)-cobalt(II) oxide (NiCo_2O_3 , $\geq 99.99\%$) were purchased from Sigma-Aldrich. Iridium oxide (IrO_x , $\geq 99.99\%$) was obtained from Alfa Aesar. Ultrapure deionized water (18 M Ω cm resistivity) used in the experiments was supplied by a Thermo Scientific Barnstead Nanopure system.

2.2. Thin film catalyst layer preparation

Prior to depositing the catalyst-ionomer film, the disk electrode (RDE/RRDE) was polished using 50 nm Al_2O_3 particle suspension on a rayon micro-cloth disk for 2–3 minutes. The catalyst ink was prepared by mixing 4 ml anhydrous ethanol, 54 μL Nafion[®] solution (5%) and 5 mg catalyst, followed by ultrasonication at room temperature for 0.5 h. Then, the formed ink was deposited on the entire surface of the disk electrode as a droplet using a 2–20 μL adjustable micro-pipette, and dried in air under an infrared lamp. The coating/drying cycles were conducted several times until the target loading (0.24 and 0.08 mg cm^{-2} deposited on RDE and RRDE, respectively) was achieved.

2.3. Physicochemical characterization

Ionic conductivity of the bulk electrolyte solution was measured by Malvern Zetasizer Nano ZS90 at room temperature. X-ray diffraction (XRD) patterns were obtained on a PANalytical X'Pert PRO with a $\text{Cu-K}\alpha$ radiation ($\lambda = 1.5406 \text{ \AA}$) at a voltage of 30 kV and a current of 10 mA.

2.4. Electrochemical characterization

All electrochemical tests were performed in a three-electrode electrochemical cell (Pine Instruments) with a Pt foil and an Hg/HgO electrode (filled with 1 M KOH) as the counter electrode and reference electrode (RE), respectively. A CHI 750E electrochemical workstation was used to conduct the electrochemical measurements with high speed and high resolution data acquisition channels. It should be emphasized that, to eliminate the chance of leaking and contamination, KOH electrolyte solution was contained in an alkaline-resistant polytetrafluoroethylene cell. Prior to testing, high-purity N_2 gas was bubbled through the electrolyte for at least 30 min to remove the dissolved O_2 . The reference electrode potential was calibrated via reversible

hydrogen electrode (RHE). In H_2 -saturated 1 M KOH, the calibrated potential we obtained was 0.898 V at room temperature. When using different concentrations of KOH, the RE potential was calibrated vs. RHE according to the following equation:

$$E_{\text{RHE}} = E_{\text{RE}} + 0.898 \text{ V} + 0.059\Delta\text{pH} \quad (1)$$

where E_{RE} is the experimental potential measured against RE, and ΔpH is the pH difference relatively to pH of 1 M KOH. After the prepared electrode was mounted onto the modulated speed rotator assembly with the electrode surface facing downward in the N_2 -saturated KOH, the CL surface was activated or cleaned by cycle voltammetry (CV) between 0.4–1.4 V at 300 mV s^{-1} until stable voltammogram curves were obtained. Then electrocatalytic properties of each studied sample were evaluated by conducting linear sweep voltammetry (LSV), electrochemical impedance spectroscopy (EIS), CV and double potential step chronoamperometry (CA).

3. Results and discussion

3.1. Electronic double layer and its functions

The EDL structure has an impact on the reaction rate of OER. As shown in Fig. 1, electrocatalytic OER is always accompanied by the EDL charging process and continuous reconstruction. The reconstruction, depending on the applied materials and electrochemical conditions, can be ascribed to the chemical and structural flexibility of the oxide catalyst interface [22]. During the EDL capacitive charging process, solvated OH^- ions are adsorbed into the inner Helmholtz plane (IHP) due to non-covalence interactions with the positive catalyst layer (CL). It is widely accepted that this capacitive behavior can qualitatively represent the available electrochemical surface area (ECSA) for OER [24–26]. Nevertheless, the measured capacitance cannot be directly correlated to ECSA since O_2 blockage, EDL reconstruction and accordingly, an excess/deficiency of OH^- adsorption might occur during the continuous electrochemical process [18,27]. These phenomena explain why the traditional CV method cannot precisely capture ECSA [16,27].

Separated from IHP by a distance of a few molecules, the outer Helmholtz plane (OHP) has opposite polarity due to non-specially adsorbed cation K^+ . The cation interaction with the charged EDL involves mainly electrostatic forces, so their interaction is essentially independent of the ionic chemical properties [18]. To balance the EDL charge, the ion distribution is extended to the diffuse layer between OHP and bulk electrolyte solution. The electric potential profiles across the EDL region are shown in Fig. 1b–d [18]. The overall applied/measured potential is a sum of several interfacial potential differences. Unfortunately, these interfacial overpotentials cannot be evaluated independently. When using a highly concentrated electrolyte solution, the overpotential due to OH^- transport in diffuse layer is minimized. Therefore, the OH^- activity in the compact Helmholtz plan is increased, which in turn, improves the efficiency of OER. As shown in Fig. 1e, less-accessible sites, such as micro-pores, corners, cracks and grain boundaries, incur additional resistance of charge transport and adsorption when compared with accessible active sites. In addition, OER generated O_2 can reside on the reaction boundaries by the Van der Waals force and block the catalyst active sites [28]. Fig. 1f schematically illustrates the complicated interactions of all species in the EDL. Due to their highly interactive nature, no single interaction among all involved species can be measured or quantified precisely.

3.2. Potential scan rate-dependent electrochemical performance

Ir oxide and Ni-Co oxide are widely used and studied as OER catalyst candidates due to their promise for large-scale applications [14,29–33]. In our previous work, we demonstrated that both the commercial Ir oxide and Ni-Co oxide (the atomic ratio $\text{Ni/Co} = 1/2$) have high OER activity and sufficient stability in the alkaline medium

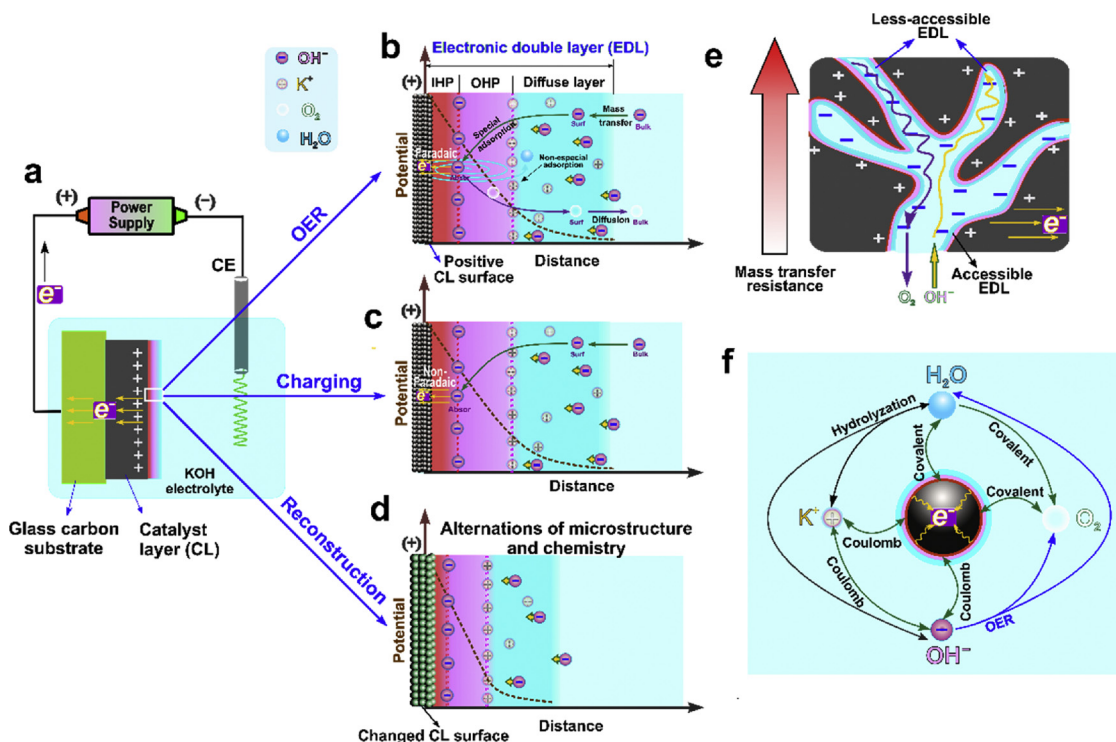


Fig. 1. Schematic representation of the aqueous-based electrochemical interfaces for electrocatalytic OER. (a) The electrochemical measurement system. GC, glassy carbon; CL, catalyst layer; CE, counter electrode. (b, c and d) Electrical double layer during OER, charging and structural and chemical reconstruction process, respectively. IHP, inner Helmholtz plane; OHP, outer Helmholtz plane (IHP). (e) Enlarged view of the electrical double layer during OER. (f) Interaction between different species during OER.

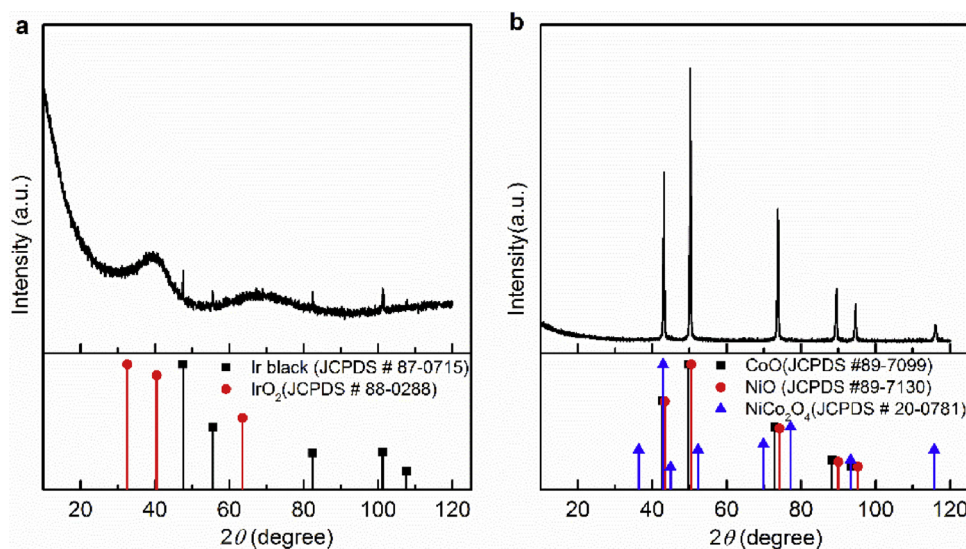


Fig. 2. XRD patterns of commercial (a) IrO_x and (b) NiCo₂O₃. Stick reference patterns are also included.

[17]. According to XRD patterns in Fig. 2, the Ir oxide sample exhibits mostly amorphous structure of IrO₂ with narrow peaks of metallic Ir phase. Meanwhile, the Ni-Co oxide shows high crystallinity matching a cubic crystal structure of NiO and CoO. Thus, the samples studied in this work are identified to be IrO_x and NiCo₂O₃.

Catalyst activity is generally evaluated through linear sweep voltammetry (LSV). Measurements were carried out in a thin-film rotating disk electrode (TF-RDE) system filled with N₂-saturated 1 M KOH solution. The rotating speed was set to 1600 rpm to provide a consistent and well-controlled testing environment. The potential scan rate ranged from 0.1 to 5.0 mV s⁻¹, which covers most published work on OER catalyst evaluation [14,17,34,35]. The initial potential is given in the

non-OER region where only EDL charging current exists. To ensure catalyst activity and repeatability, the measured LSV results from each scan rate were obtained from newly prepared electrodes.

As shown in Fig. 3a,b, the current density increases exponentially when the applied potential exceeds the onset OER potential, i.e., approximately 1.475 V for IrO_x and 1.50 V for NiCo₂O₃. Moreover, the detected current density increases with increasing scan rate for IrO_x, while the trend for NiCo₂O₃ is reversed. These are the first reported data of an OER catalyst that shows current density decreasing with scan rate.

The reverse trend is further demonstrated by the IR-free Tafel plots in Fig. 3c,d. The fitted Tafel slopes indicates that the potential scan rate

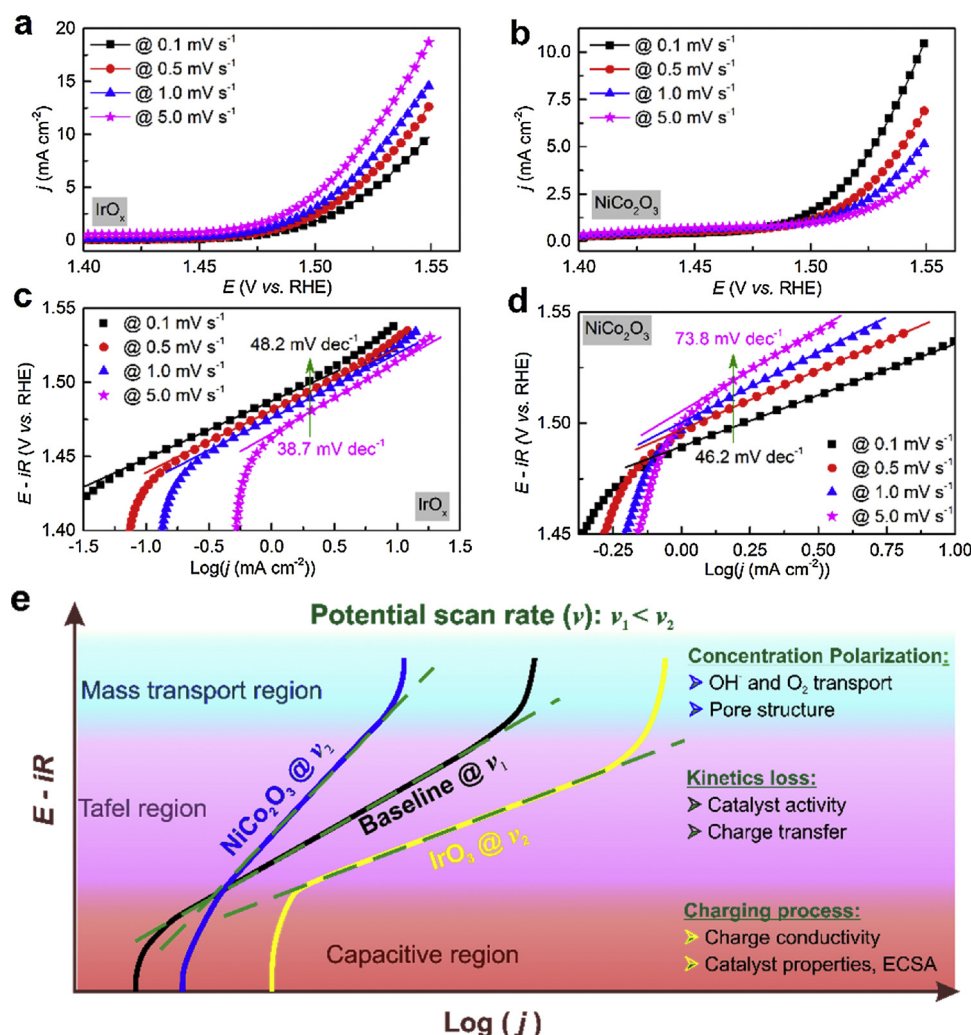


Fig. 3. Evaluation of electrocatalytic performance via TF-RDE LSV with various scan rates in 1 M KOH. (a, b) LSV plots of IrO_x and NiCo₂O₃, respectively. (c, d) IR-corrected Tafel plots of IrO_x and NiCo₂O₃, respectively. Arrow represents the direction of increasing Tafel slopes. Symbols - raw data; lines - linear fit to the data. (e) Schematic representation of Tafel plots with potential scan rates.

has an obvious effect both on the charging process and OER kinetics. Fig. 3e illustrates the performance change and lists fundamental mechanisms of capacitive, kinetics-controlled Tafel, and mass transport regions. Meanwhile, similar LSV measurements were conducted in acid media (Fig. S1, refer to Supplementary Materials, SM). However, the reverse trend with scan rate is not observed for OER in acidic media, which is based on H⁺ adsorption. This result indicates that the alkaline media are mainly responsible for the reverse trend. In aqueous electrolyte, OH⁻ ion has a much greater size and lower ionic conductivity than H⁺ [36]. In addition, for alkaline OER, OH⁻ are specially adsorbed in the IHP as a reactant, while for acidic OER, H⁺ is a non-specially adsorbed byproduct. Therefore the inner Faradaic reaction in alkaline media is highly sensitive to the scan-rate-dependent OH⁻ adsorption and transfer.

3.3. Charging current contribution and O₂ transport effects

Further evaluations via TF-RRDE voltammetry were performed to study the charging capacitive current contribution and efficient O₂ transport in EDL [17]. Instead of 1 M KOH used in the TF-RDE study, 6 M KOH electrolyte solution was used for the TF-RRDE measurements to minimize ionic resistance in the bulk solution. The ionic conductivities of 1 M and 6 M KOH electrolyte are measured to be 232 and 552 mS cm⁻¹, respectively, using a Zetasizer from Malvern

Instruments, Inc. To further accelerate species and charge transport in EDL, the electrode rotating speed was increased from 1600 to 2500 rpm. Further, the catalyst loading is reduced from 0.24 to 0.08 mg cm⁻² to minimize performance loss due to active site overlap. Based on these modifications, it is expected that the obtained electrochemical results can better reflect the intrinsic properties of the reaction interface.

A schematic of the TF-RRDE configuration is shown in Fig. 4a. The disk potential ranges from 1.4 to 1.55 V, while the potential of the Pt-ring is held constant at 0.4 V to detect oxygen reduction reaction (ORR). The performance trend with respect to scan rate observed from TF-RRDE shown in Fig. S2 (refer to SM) is identical to that from TF-RDE. The measured TF-RRDE data are processed by our newly-developed methods to obtain the capacitive current ratio, ϵ_c , and O₂ transport efficiency, ϵ_{O_2} [17]. As shown in Fig. 4b, IrO_x has higher ϵ_c than NiCo₂O₃ at a given scan rate. This increase of the capacitive contribution caused by OH⁻ adsorption can facilitate OER in the Tafel region.

As the applied potential grows, the contribution of the charging current decays and the detected disk current increases primarily because of the faster OER rate. O₂ transport efficiency in EDL becomes an essential parameter in determining available active reaction sites. Although the fast spinning electrode and diffusion driving force facilitate efficient O₂ removal, the actual rate still depends on the catalyst and its microstructure. Due to the proximity of the ring electrode, it is

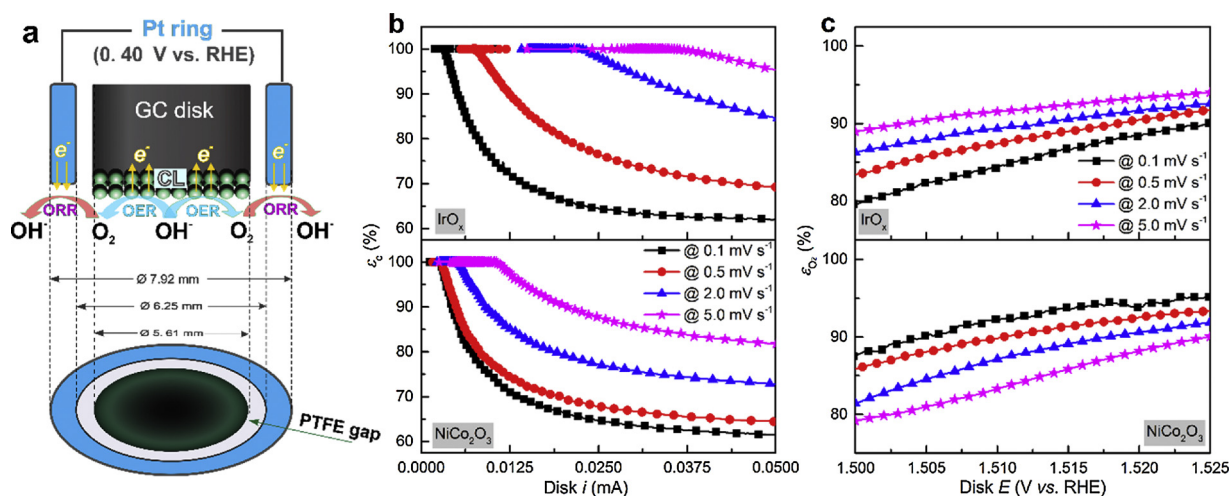


Fig. 4. TF-RRDE voltammogram evolution in 6 M KOH. (a) Schematic illustration of the TF-RRDE configuration, (b) EDL charging capacitive current ratio, and (c) O_2 transport efficiency at the different potential scan rates.

assumed that O_2 trapped in the disk can be reduced back to OH^- . Under this assumption, O_2 transport efficiency, ε_{O_2} , can be evaluated by the net ORR current at the ring. Meanwhile, the ring potential is adjusted to 1.4 V for detecting HO_2^- intermediates generated from 2-electron transfer reactions. The results shown in Fig. S3 (refer to SM) confirms that nearly no HO_2^- is formed in the disk during the OER process.

As seen in Fig. 4c, a reverse trend is again observed for ε_{O_2} of both catalysts. In the studied scan rate range of 0.1–5.0 $mV s^{-1}$, the O_2 transport efficiency increases from 80% to 90% for IrO_x , but drops from 90% to 80% for $NiCo_2O_3$ at 1.5 V. OER performance can be enhanced by increasing the O_2 transport efficiency in EDL. Therefore, O_2 transport efficiency can be considered a crucial factor to explain the trends observed in Fig. 3. In general, such transport behavior is directly related to the interaction between generated O_2 and the EDL microstructure [19]. This suggests that the EDL microstructure is being reconstructed during the continuous OER process, and the reconstruction depends on potential scan rate.

3.4. Intrinsic properties of reaction interface

After TF-RRDE voltammetry measurements, EIS is performed immediately to further study the EDL structural and electrochemical characteristics. EIS data shown in Fig. 5a are simulated by an equivalent circuit $LR_{ct}(R_{ct}C_1)(R_1C_2)$ (Fig. 5b). The key elements to determining interfacial properties involve ohmic resistance (R_{Ω}), total polarization resistance ($R_{ct} + R_1$) and EDL capacitance (C_{EDL}).

The ohmic resistances of IrO_x and $NiCo_2O_3$, in Table S1, are 0.6 and 0.8 Ωcm^2 , respectively. For $NiCo_2O_3$, the increased electron transport resistance may delay EDL potential equilibrium, especially at high scan rates, causing a reduction in steady-state OER performance. Based on our previous work, the ECSA from in-situ EIS data can be obtained with accuracy [17]. The calculated ECSA of $NiCo_2O_3$ is about 35 $m^2 g^{-1}$, which is 44% less than that of IrO_x .

After various scan rates of LSV measurements, EIS data show that the ohmic resistance and EDL capacitance remain relatively unchanged, but polarization resistance ($R_{ct} + R_1$) exhibits significant difference. In the case of $NiCo_2O_3$, $R_{ct} + R_1$ listed in Table S1 is much lower after the 0.1 $mV s^{-1}$ LSV test (1.677 Ωcm^2) than that after 5.0 $mV s^{-1}$ (3.591 Ωcm^2). This observation confirms the activity enhancement of $NiCo_2O_3$ using the lower scan rate, which suggests that $NiCo_2O_3$ requires a longer time to activate the reaction interface. It is deduced that beneficial modifications of the surface chemical state take place during the dynamic potential-scan operation. In contrast, IrO_x exhibited increased

$R_{ct} + R_1$ after the high-scan-rate LSV. Fig. 3a clearly shows the improved OER performance as scan rate increases, which should yield less $R_{ct} + R_1$. Therefore, the EIS results of IrO_x indicate that the increased OER current at high scan rate can accelerate degradation of the active interface. According to Cherevko et al., the dissolution rate of Ir-based catalysts increases linearly with oxygen evolution current [37].

The CV curves with various scan rates in Fig. S5 reveal the unique characteristics of the active metal redox and EDL charging capacitive processes. From Fig. 5c,d, the EDL charging capacitive current density (j_c) increases with scan rate (ν). However, unlike the linear relationship between j_c and ν , $NiCo_2O_3$ shows a trend of logarithmic growth of j_c . This is because α/β -phase Ni^{2+} (or Co^{2+}) hydroxide can significantly suppress capacitive behavior due to poor electrical conduction [38,39].

EDL capacitance, C_{EDL} , is calculated by $|j_c|/\nu$ (refer to SM). The ratio of C_{EDL} to the total capacitance C_{total} at a given scan rate embodies the nature of the material porosity and surface electron conductivity [24,40] and is plotted on the secondary y-axis in Fig. 5c,d. It appears that C_{EDL}/C_{total} remains relatively unchanged for IrO_x and decreases for $NiCo_2O_3$ with increasing scan rate. This is because $NiCo_2O_3$ has low electrical conductivity and a high percentage of less-accessible EDL. The XRD patterns in Fig. 2b reveal that the Ni-Co oxide exists in the form of MO ($M = Ni/Co$), which spontaneously transforms to hydrated α - and/or β - $M(OH)_2$ in aqueous KOH. The α/β -hydroxide behaves like an insulator and has very low electrical conductivity [39,41]. The less-accessible EDLs might be available at low scan rates, but not at higher scan rates. As a result, less than 10% of C_{total} is detected at over 200 $mV s^{-1}$ for $NiCo_2O_3$. According to the low-temperature N_2 adsorption-desorption isotherm tests shown in Table S2, $NiCo_2O_3$ has lower BET surface area, total pore volume and average pore size than IrO_x . The ex-situ data, combined with the in-situ CV and LSV observations, imply that there is increased resistance to charge transfer and O_2 transport in the reaction interface.

Pseudocapacitance, which can provide qualitative information about less-accessible active sites for OER [25,42,43], is characterized by the redox peaks shown in Fig. S5. In principle, the redox rate is determined by reaction kinetics at low scan rates. In contrast, charge and mass transports become the dominating factors at high scan rates. Oxidation peaks were reported to be around 0.65 V and 1.3 V for IrO_x and $NiCo_2O_3$, respectively, in our recent work [17]. After subtracting the EDL charging capacitive current at 0.9 V from the collected oxidation peak current, the net Faradaic peak current is further processed to obtain the C_{EDL} -free pseudocapacitance per mole of electrochemical active species (C_M). It is observed from Fig. 5e that the basic tendency of C_M decreases with scan rate for both catalysts because of the

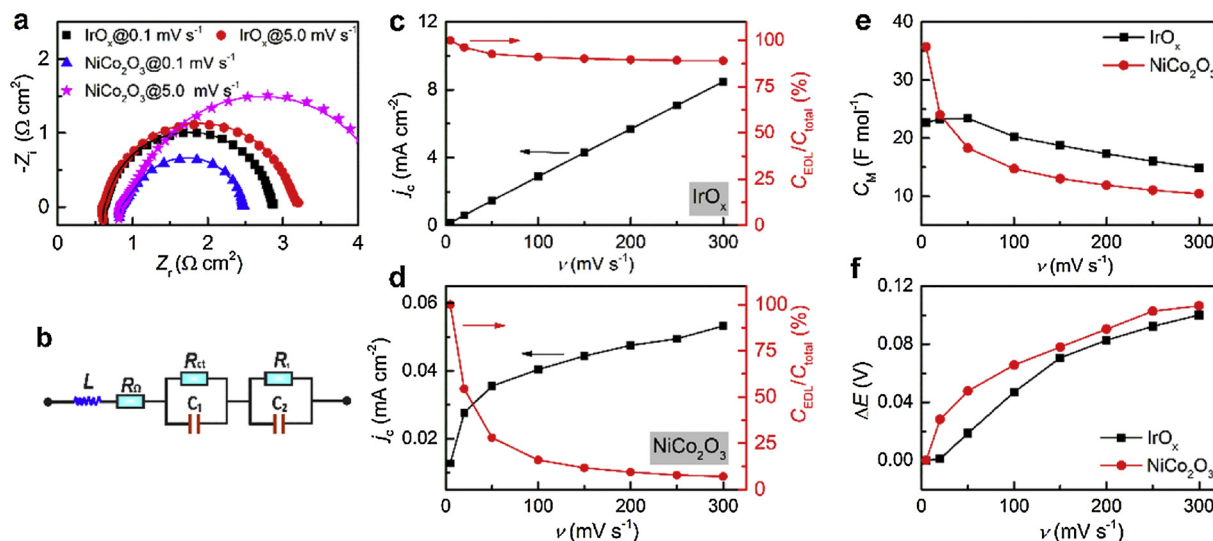


Fig. 5. Intrinsic property evaluation in 6 M KOH. (a) EIS spectra of IrO_x and NiCo₂O₃ at 1.55 V after scan-rate-depending LSV tests. Symbols – raw data; lines – linear fit to the data. (b) The equivalent circuit used for simulating EIS. (c and d) EDL charging capacitive current density (left) and the ratio of EDL charging capacitance (C_{EDL}) to total charging capacitance (C_{total}) (right). (e) The net Faradaic peak pseudocapacitance (C_M), and (f) potential shift (ΔE) of Faradaic oxidation peak as a function of CV scan rate. The oxidation reaction observed in CV curves is $Ir^{2+} \rightarrow Ir^{3+}$ (for IrO₂) or $M^{2+} \rightarrow M^{3+}$ ($M = Ni/Co$, for NiCo₂O₃).

existence of less-accessible active sites and less total time required for each scan rate. When scan rate is below 50 mV s⁻¹, the C_M of IrO_x reaches maximum, suggesting facile electron and OH⁻ transports in the EDL. For NiCo₂O₃, the C_M reduces much more than that for IrO_x, indicating extra resistance to pseudocapacitive charging during the potential scan process. The peak potential shift as a function of scan rate can be attributed to slow electron transfer kinetics at low scan rate and mass transport at high scan rate. Compared with IrO_x, in Fig. 5f, NiCo₂O₃ exhibits a larger shift of the peak potential especially at the low scan rate, indicating sluggish redox kinetics.

3.5. EDL reconstruction and its mechanism

To further study the transient features on EDL reconstruction, double potential step chronoamperometry (CA) is conducted in the TF-RRDE system. The major experimental parameters are shown in Fig. 6a. During the short testing time of 8 min, the observed performance difference can be attributed to EDL modification, since sufficient electrochemical stability of IrO_x and NiCo₂O₃ has been demonstrated in our previous work [17]. During CA measurement, there were four instant voltage increases (steps 1, 3, 5, and 7) and four instant voltage drops (steps 2, 4, 6, and 8). At 1.45 V, the measured disk current results mainly from the charging capacitive process, as indicated by the minimal Faradaic OER current in Fig. S6 (refer to SM). In contrast to IrO_x, NiCo₂O₃ shows a continuous increasing double layer charge current ratio, ϵ_c , from step 2 to 8 in Fig. 6b. This trend confirms that NiCo₂O₃ requires more time to achieve higher pseudocapacitive performance. The cubic crystal structure of NiCo₂O₃ experiences phase transformation from α -M(OH)₂ to β -M(OH)₂ during the continuous testing processes, which significantly enhances the electrical conductivity and accordingly, redox reaction M^{2+}/M^{3+} . As for amorphous IrO_x, the hybrid current at 1.45 V is generated due to the redox reaction of active Ir species and EDL charging capacitive process. In the CA testing process, active sites can be oxidized to higher oxidation states such as Ir⁵⁺ and Ir⁶⁺, which is thermodynamically unstable at the OER potential. It has been reported that the higher Ir oxidation states suppress the EDL capacitive behavior [34,44]. Therefore, the decrease of charge current ratio from step 2 to step 8 can be ascribed to the formation of higher Ir oxidation states. Further, at every step, it appears that IrO_x takes a longer time to achieve steady state than NiCo₂O₃. This may be due to the increased number of generated O₂ and adsorbed

charges accompanied by higher OER rate.

When the applied potential rises instantaneously from 1.45 V to 1.525 V in Fig. 6c, IrO_x current decreases from 1.02 mA (step 1) to 0.75 mA (step 7), while NiCo₂O₃ increases by 0.16 mA. Similar trends can be observed in Fig. 6d, indicating that O₂ transport efficiency is a crucial parameter in determining OER performance. These changes occurring in each testing step can be attributed to EDL reconstruction, which determines the charging capacitive process and electrocatalytic OER.

Depending on the applied materials, reconstruction can occur through different mechanisms as illustrated in Fig. 7 [27,41,44–48]. The oxide interface has the structural and chemical flexibility needed for microscale reconstruction. In alkaline solution, the metal oxide surfaces are hydrophilic, leading to the hydroxylation of surface oxygen groups. The hydroxylation process at the reaction interface has been recognized as a key step for catalyst activation [19]. In principle, OER takes place by a cyclic transition of hydroxylated metal cations with different oxidation states [44,49]. Table S1 indicates that the measured ECSA of both catalysts remains unchanged after LSV tests at 0.1 and 5.0 mV s⁻¹. This suggests minimal bulk structural change during continuous electrochemical measurements.

For IrO_x, the cyclic transition of metal cations is Ir⁵⁺/Ir³⁺, and the same intermediate, Ir³⁺, is also observed for catalyst dissolution [25]. In comparison with the rutile-type IrO₂, the hydrated amorphous IrO_x experiencing high OER activity can facilitate the phase transition toward deeper hydration and higher oxidation states due to the enhancement of unsaturated sites and chemical flexibility [48,50]. It is noted that metal cations with higher oxidation states such as Ir⁶⁺, which can be formed at the applied OER potential, have lower OER activity and stability than metal cations with lower valence, like Ir³⁺ and Ir⁴⁺ [34,37,45]. Meanwhile, intermediate Ir⁵⁺ can also accelerate Ir dissolution by transforming to Ir⁶⁺ or Ir³⁺ in the alkaline condition. According to the CV results in Fig. S5a, hydrous Ir³⁺ is formed at a potential around 0.65 V prior to OER. Therefore, the performance degradation during continuous CA steps can be attributed to Ir dissolution and the formation of higher oxidation states. Conversely, in the case of the cubic NiCo₂O₃, there are four metal hydroxide phases known to be present near the oxygen evolution reaction potential: α -M(OH)₂, β -M(OH)₂, β -MOOH and γ -MOOH [39]. The β -MOOH/ γ -MOOH transformation has been caused by further oxidation of β -MOOH [51,52]. Due to the high crystalline and reversible features, the interfacial phase

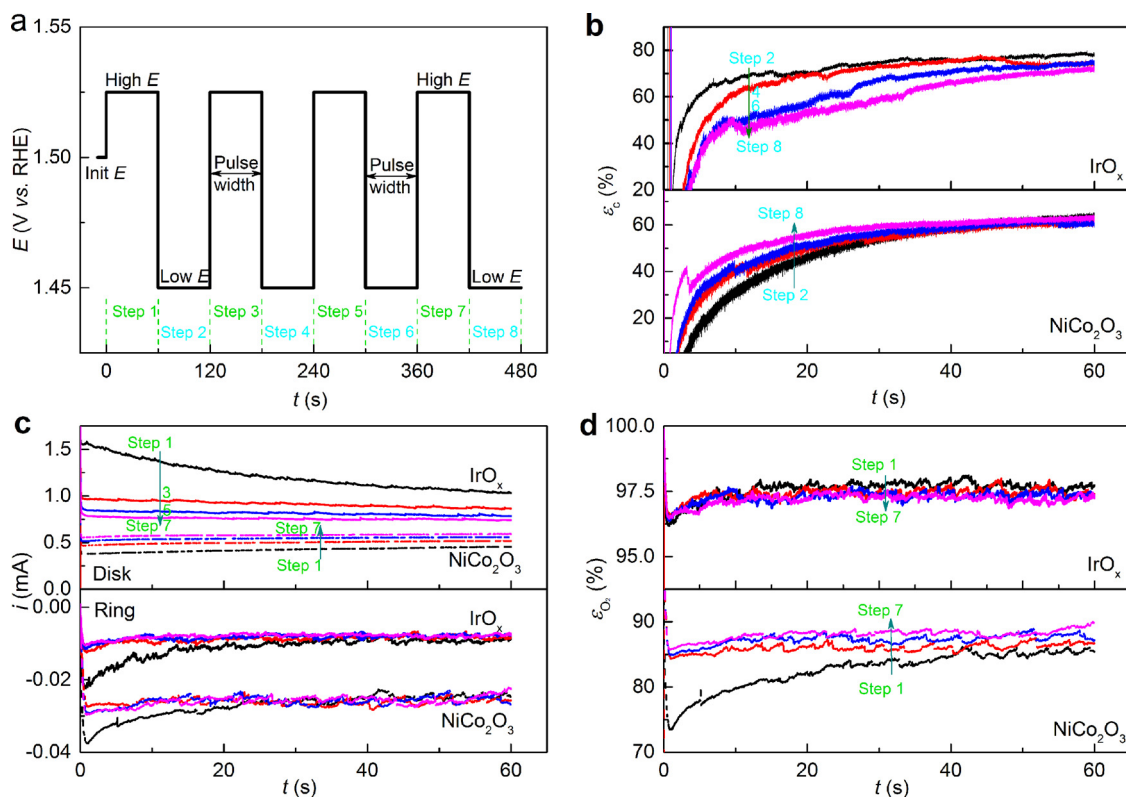


Fig. 6. TF-RRDE chronoamperometry evolution in 6 M KOH. (a) Diagram of chronoamperometry with major experimental parameters, (b) Charging capacitive current contribution (i_c) to the disk current in steps 2, 4, 6 and 8 at a disk potential of 1.45 V, (c) TF-RRDE chronoamperometry curves in steps 1, 3, 5 and 7 at a disk potential of 1.525 V, and (d) O_2 transport efficiency (ε_{O_2}) in steps 1, 3, 5 and 7.

transition toward the enhanced performance is likely to take place across the entire measurement process. Although a higher valence state, like M^{5+} , can accelerate oxide dissolution, the required potential to form a higher valence state is higher than the applied potential in this work. Therefore, increasing testing time can boost the performance of Ni-Co oxide. In summary, the opposite trend of LSV curves as a function of scan rate observed from IrO_x and NiCo_2O_3 can be attributed to material intrinsic features and EDL reconstruction during the continuous measurement process.

4. Conclusions

Herein, the EDL effect on electrocatalytic OER is studied extensively by electrochemical characterization. The catalyst activity obtained from the typical LSV method shows a strong dependency on scan rate due to distinct EDL behaviors such as the charging process, kinetics-controlled reactions, mass transport, and EDL reconstruction. The measured OER performance increases with increasing scan rate for IrO_x and the trend

is reversed for NiCo_2O_3 . Further characterization reveals that this opposite trend is caused by the materials' intrinsic structural and chemical features as well as drastic interfacial reconstruction during OER. In particular, the CA data show that the continuous EDL reconstruction is favorable for OH^- adsorption and OER for NiCo_2O_3 . However, using IrO_x , the result is opposite due to Ir dissolution and the formation of higher oxidation state. The findings of this work provide valuable information to accurately characterize catalyst performance, EDL structure and electrochemical behaviors, and the EDL modifications during continuous electrochemical measurements and the OER process.

Conflict of interest

The authors declare no competing financial interests.

Acknowledgements

The authors would like to thank Professor Ashlie Martini for

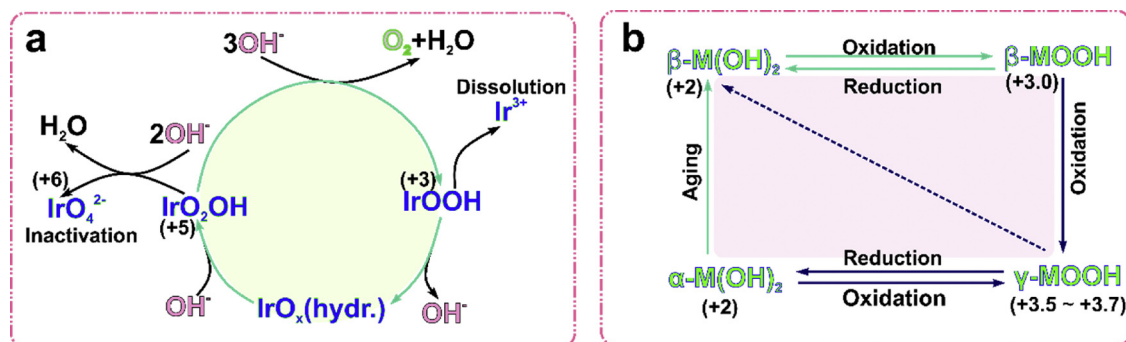


Fig. 7. Schematic illustration of EDL reconstruction for (a) IrO_x and (b) NiCo_2O_3 (M = Ni/Co) during the capacitive charging and OER process.

reviewing our work. This study is co-sponsored by University of California, Merced, and GreenPower Program (IIID 2015-09) of the Commission on Higher Education – Philippine California Advanced Research Institutes (CHED-PCARI), Republic of the Philippines.

Appendix A. Supplementary data

Supplementary material related to this article can be found, in the online version, at doi:<https://doi.org/10.1016/j.apcatb.2018.08.037>.

References

- [1] J. Rosen, Arctic 2.0: what happens after all the ice goes? *Nature* 542 (2017) 152–154.
- [2] P. Kruger, Electric power requirement in California for large-scale production of hydrogen fuel, *Int. J. Hydrogen Energy* 25 (2000) 395–405.
- [3] X. Ge, A. Sumboja, D. Wu, T. An, B. Li, F.W.T. Goh, T.S.A. Hor, Y. Zong, Z. Liu, Oxygen reduction in alkaline media: from mechanisms to recent advances of catalysts, *ACS Catal.* 5 (2015) 4643–4667.
- [4] S. Jung, C.C.L. McCrory, I.M. Ferrer, J.C. Peters, T.F. Jaramillo, Benchmarking nanoparticulate metal oxide electrocatalysts for the alkaline water oxidation reaction, *J. Mater. Chem. A Mater. Energy Sustain.* 4 (2016) 3068–3076.
- [5] J.R. Varcoe, P. Atanassov, D.R. Dekel, A.M. Herring, M.A. Hickner, P.A. Kohl, A.R. Kucernak, W.E. Mustain, K. Nijmeijer, K. Scott, T. Xu, L. Zhuang, Anion-exchange membranes in electrochemical energy systems, *Energy Environ. Sci.* 7 (2014) 3135–3191.
- [6] J.X. Feng, S.H. Ye, H. Xu, Y.X. Tong, G.R. Li, Design and synthesis of FeOOH/CeO₂ heterolayered nanotube electrocatalysts for the oxygen evolution reaction, *Adv. Mater.* 28 (2016) 4698–4703.
- [7] J.X. Feng, H. Xu, Y.T. Dong, S.H. Ye, Y.X. Tong, G.R. Li, FeOOH/Co/FeOOH Hybrid Nanotube Arrays as High-Performance Electrocatalysts for the Oxygen Evolution Reaction, *Angew. Chem. Int. Ed.* 55 (2016) 3694–3698.
- [8] M. Favaro, J. Yang, S. Nappini, E. Magnano, F.M. Toma, E.J. Crumlin, J. Yano, I.D. Sharp, Understanding the oxygen evolution reaction mechanism on CoOx using operando ambient pressure X-ray photoelectron spectroscopy, *J. Am. Chem. Soc.* 139 (2017) 8960–8970.
- [9] Y. Jiao, Y. Zheng, M. Jaroniec, S.Z. Qiao, Design of electrocatalysts for oxygen- and hydrogen-involving energy conversion reactions, *Chem. Soc. Rev.* 44 (2015) 2060–2086.
- [10] Y. Chen, F. Mojica, G. Li, P.-Y.A. Chuang, Experimental study and analytical modeling of an alkaline water electrolysis cell, *Int. J. Energy Res.* 41 (2017) 2365–2373.
- [11] S.H. Ye, Z.X. Shi, J.X. Feng, Y.X. Tong, G.R. Li, Activating CoOOH porous nanosheet arrays by partial Iron substitution for efficient oxygen evolution reaction, *Angew. Chem. Int. Ed.* 57 (2018) 2672–2676.
- [12] Y. Leng, G. Chen, A.J. Mendoza, T.B. Tighe, M.A. Hickner, C.Y. Wang, Solid-state water electrolysis with an alkaline membrane, *J. Am. Chem. Soc.* 134 (2012) 9054–9057.
- [13] I. Vincent, D. Bessarabov, Low cost hydrogen production by anion exchange membrane electrolysis: a review, *Renew. Sustain. Energy Rev.* 81 (2018) 1690–1704.
- [14] R. Frydendal, E.A. Paoli, B.P. Knudsen, B. Wickman, P. Malacrida, I.E.L. Stephens, I. Chorkendorff, Benchmarking the stability of oxygen evolution reaction catalysts: the importance of monitoring mass losses, *ChemElectroChem* 1 (2014) 2075–2081.
- [15] C.C. McCrory, S. Jung, I.M. Ferrer, S.M. Chatman, J.C. Peters, T.F. Jaramillo, Benchmarking hydrogen evolving reaction and oxygen evolving reaction electrocatalysts for solar water splitting devices, *J. Am. Chem. Soc.* 137 (2015) 4347–4357.
- [16] C.C.L. McCrory, S. Jung, J.C. Peters, T.F. Jaramillo, Benchmarking heterogeneous electrocatalysts for the oxygen evolution reaction, *J. Am. Chem. Soc.* 135 (2013) 16977–16987.
- [17] G. Li, L. Anderson, Y. Chen, M. Pan, P.-Y. Abel Chuang, New insights into evaluating catalyst activity and stability for oxygen evolution reactions in alkaline media, *Sustain. Energy Fuels* 2 (2018) 237–251.
- [18] A.J. Bard, L.R. Faulkner, *Electrochemical methods, Fundamentals and Applications*, 2nd edition, John Wiley & Sons, Inc., 2001.
- [19] R.L. Doyle, M.E.G. Lyons, The oxygen evolution reaction: mechanistic concepts and catalyst design, in: S. Giménez, J. Bisquert (Eds.), *Photoelectrochemical Solar Fuel Production: From Basic Principles to Advanced Devices*, Springer International Publishing, Cham, 2016, pp. 41–104.
- [20] N. Danilovic, R. Subbaraman, K.-C. Chang, S.H. Chang, Y.J. Kang, J. Snyder, A.P. Paulikas, D. Strmcnik, Y.-T. Kim, D. Myers, V.R. Stamenkovic, N.M. Markovic, Activity–stability trends for the oxygen evolution reaction on monometallic oxides in acidic environments, *J. Phys. Chem. Lett.* 5 (2014) 2474–2478.
- [21] Z. Zeng, K.-C. Chang, J. Kubal, N.M. Markovic, J. Greeley, Stabilization of ultrathin (hydroxy)oxide films on transition metal substrates for electrochemical energy conversion, *Nat. Energy* 2 (2017) 17070.
- [22] J. Chakhalian, A.J. Millis, J. Rondinelli, Whither the oxide interface, *Nat. Mater.* 11 (2012) 92–94.
- [23] J.H. Bae, J.-H. Han, T.D. Chung, Electrochemistry at nanoporous interfaces: new opportunity for electrocatalysis, *Phys. Chem. Chem. Phys.* 14 (2012) 448–463.
- [24] S. Ardizzone, G. Fregonara, S. Trasatti, Inner and outer active surface of RuO₂ electrodes, *Electrochim. Acta* 35 (1990) 263–267.
- [25] A. Eftekhari, From pseudocapacitive redox to intermediary adsorption in oxygen evolution reaction, *Mater. Today Chem.* 4 (2017) 117–132.
- [26] S. Trasatti, O.A. Petrii, In electrochemistry, *J. Electroanal. Chem.* 327 (1992) 353–376.
- [27] A. Ganassin, A. Maljusch, V. Colic, L. Spanier, K. Brandl, W. Schuhmann, A. Bandarenka, Benchmarking the performance of thin-film oxide electrocatalysts for gas evolution reactions at high current densities, *ACS Catal.* 6 (2016) 3017–3024.
- [28] D. Zhang, K. Zeng, Evaluating the behavior of electrolytic gas bubbles and their effect on the cell voltage in alkaline water electrolysis, *Ind. Eng. Chem. Res.* 51 (2012) 13825–13832.
- [29] F.-X. Ma, L. Yu, C.-Y. Xu, X.W. Lou, Self-supported formation of hierarchical NiCo₂O₄ tetragonal microtubes with enhanced electrochemical properties, *Energy Environ. Sci.* 9 (2016) 862–866.
- [30] X. Gao, H. Zhang, Q. Li, X. Yu, Z. Hong, X. Zhang, C. Liang, Z. Lin, Hierarchical NiCo₂O₄ hollow microcuboids as bifunctional electrocatalysts for overall water-splitting, *Angew. Chem. Int. Ed.* 55 (2016) 6290–6294.
- [31] L. Wang, C. Lin, D. Huang, F. Zhang, M. Wang, J. Jin, A comparative study of composition and morphology effect of Ni_xCo_{1-x}(OH)₂ on oxygen evolution/reduction reaction, *ACS Appl. Mater. Interfaces* 6 (2014) 10172–10180.
- [32] X. Li, X. Hao, A. Abudula, G. Guan, Nanostructured catalysts for electrochemical water splitting: current state and prospects, *J. Mater. Chem. A Mater. Energy Sustain.* 4 (2016) 11973–12000.
- [33] B. Cui, H. Lin, J.B. Li, X. Li, J. Yang, J. Tao, Core-ring structured NiCo₂O₄ nanoplatelets: synthesis, characterization, and electrocatalytic applications, *Adv. Funct. Mater.* 18 (2008) 1440–1447.
- [34] G. Li, H. Yu, X. Wang, S. Sun, Y. Li, Z. Shao, B. Yi, Highly effective Ir_xSn_{1-x}O₂ electrocatalysts for oxygen evolution reaction in the solid polymer electrolyte water electrolyser, *Phys. Chem. Chem. Phys.* 15 (2013) 2858–2866.
- [35] F. Song, X.L. Hu, Exfoliation of layered double hydroxides for enhanced oxygen evolution catalysis, *Nat. Commun.* 5 (2014) 4477.
- [36] C. Zhong, Y. Deng, W. Hu, J. Qiao, L. Zhang, J. Zhang, A review of electrolyte materials and compositions for electrochemical supercapacitors, *Chem. Soc. Rev.* 44 (2015) 7484–7539.
- [37] S. Cherevko, S. Geiger, O. Kasian, A. Mingers, K.J.J. Mayrhofer, Oxygen evolution activity and stability of iridium in acidic media. Part 2. – electrochemically grown hydrous iridium oxide, *J. Electroanal. Chem.* 774 (2016) 102–110.
- [38] C. Costentin, T.R. Porter, J.-M. Savéant, Conduction and reactivity in heterogeneous-molecular catalysis: new insights in water oxidation catalysis by phosphate cobalt oxide films, *J. Am. Chem. Soc.* 138 (2016) 5615–5622.
- [39] D.S. Hall, D.J. Lockwood, C. Bock, B.R. MacDougall, Nickel hydroxides and related materials: a review of their structures, synthesis and properties, *Proc. R. Soc. A* 471 (2015).
- [40] J. Gaudet, A.C. Tavares, S. Trasatti, D. Guay, Physicochemical characterization of mixed RuO₂-SnO₂ solid solutions, *Chem. Mater.* 17 (2005) 1570–1579.
- [41] M. Merrill, M. Worsley, A. Wittstock, J. Biener, M. Stadermann, Determination of the “NiOOH” charge and discharge mechanisms at ideal activity, *J. Electroanal. Chem.* 717–718 (2014) 177–188.
- [42] S. Fierro, E. Passas-Lagos, E. Chatzisympson, D. Mantzavinos, C. Comninellis, Pseudo-potentiostatic electrolysis by potential buffering induced by the oxygen evolution reaction, *Electrochem. Commun.* 11 (2009) 1358–1361.
- [43] V. Augustyn, P. Simon, B. Dunn, Pseudocapacitive oxide materials for high-rate electrochemical energy storage, *Energy Environ. Sci.* 7 (2014) 1597–1614.
- [44] C. Spoori, J.T.H. Kwan, A. Bonakdarpour, D. Wilkinson, P. Strasser, The stability challenges of oxygen evolving catalysts: towards a common fundamental understanding and mitigation of catalyst degradation, *Angew. Chem.* 56 (2017) 5994–6021.
- [45] A. Grimaud, A. Demortière, M. Saubane, W. Dachraoui, M. Duchamp, M.-L. Doublet, J.-M. Tarascon, Activation of surface oxygen sites on an iridium-based model catalyst for the oxygen evolution reaction, *Nat. Energy* 2 (2016) 16189.
- [46] Z. Pavlovic, C. Ranjan, M. van Gastel, R. Schlögl, The active site for the water oxidizing anodic iridium oxide probed through in situ Raman spectroscopy, *Chem. Commun.* 53 (2017) 12414–12417.
- [47] S. Cherevko, S. Geiger, O. Kasian, A. Mingers, K.J.J. Mayrhofer, Oxygen evolution activity and stability of iridium in acidic media. Part 1. – metallic iridium, *J. Electroanal. Chem.* 773 (2016) 69–78.
- [48] Z.-H. Zhou, W. Sun, W.Q. Zaman, L.-M. Cao, J. Yang, Highly active and stable synergistic Ir–IrO₂ electro-catalyst for oxygen evolution reaction, *Chem. Eng. Commun.* 205 (2018) 966–974.
- [49] C.N. Brodsky, R.G. Hadt, D. Hayes, B.J. Reinhart, N. Li, L.X. Chen, D.G. Nocera, In situ characterization of cofacial Co(IV) centers in Co₄O₄ cubane: modeling the high-valent active site in oxygen-evolving catalysts, *Proc. Natl. Acad. Sci.* 114 (2017) 3855–3860.
- [50] G.F. Li, H.M. Yu, X.Y. Wang, D.L. Yang, Y.K. Li, Z.G. Shao, B.L. Yi, Triblock polymer mediated synthesis of Ir-Sn oxide electrocatalysts for oxygen evolution reaction, *J. Power Sources* 249 (2014) 175–184.
- [51] D.M. Sayed, G.A. El-Nagar, S.Y. Sayed, B.E. El-Anadoul, M.S. El-Deab, Activation/deactivation behavior of nano-NiOx based anodes towards the OER: influence of temperature, *Electrochim. Acta* 276 (2018) 176–183.
- [52] D.K. Bediako, B. Lassalle-Kaiser, Y. Surendranath, J. Yano, V.K. Yachandra, D.G. Nocera, Structure–activity correlations in a nickel–Borate oxygen evolution catalyst, *J. Am. Chem. Soc.* 134 (2012) 6801–6809.